Examining the Influence of Wind and Wind Wave Turbulence on Tidal Currents, Using a Three-Dimensional Hydrodynamic Model Including Wave–Current Interaction

A. M. DAVIES

Proudman Oceanographic Laboratory, Bidston Observatory, Birkenhead, Merseyside, United Kingdom

J. LAWRENCE

MAFF Fisheries Laboratory, Pakefield Road, Lowestoft, Suffolk, United Kingdom

(Manuscript received 29 June 1993, in final form 13 January 1994)

ABSTRACT

This paper presents a very brief overview of the development of a three-dimensional hydrodynamic model involving a flow-dependent eddy viscosity and including enhancements of bottom friction due to wave–current interaction in shallow water. The main point of the paper is to examine the physical nature of the process. Consequently, references to published work are given for the background detail.

Calculations using both tidal and wind forcing show that tidal elevation amplitude and phase are significantly changed in shallow near-coastal regions due to enhanced frictional effects associated with wind-driven flow and wind wave turbulence.

An analysis of tidal current profiles, at the fundamental harmonic and higher harmonics, computed with tidal and wind forcing, shows that significant changes in tidal current profiles can occur due to coupling between the wind-induced current shear and a time-evolving viscosity. The importance of the nonlinearity produced by a surface wind-induced shear and a flow-dependent viscosity in influencing tidal current profiles is confirmed using a single point model in the vertical.

1. Introduction

The influence of various formulations of vertical eddy viscosity in three-dimensional hydrodynamic models upon tidal current profiles in shallow seas has been extensively studied in a range of sea areas from continental shelf (Davies 1986) to limited areas (e.g., the Celtic and Irish Sea, Davies and Jones 1992a). In some cases high-resolution (of order 1 km) finite difference grids have been used in near-coastal regions (Aldridge and Davies 1993) to examine in detail the profile of tidal currents.

A similar range of models from shelf (Davies 1982; Davies and Flather 1987), Celtic Sea (Davies and Jones 1992b), to limited area (Proctor 1981, 1987; Davies and Lawrence 1994) have been used to examine the wind-induced residual flow in a region.

When modeling purely tidal flow it is common to run the model for the (dominant) M_2 component alone (Aldridge and Davies 1993) although other components of the tide do contribute to tidal turbulence (Le Provost and Fornerino 1985).

For wind-driven flows in shallow tidally dominated coastal seas, the usual practice is to include the tide within the wind-driven simulation in order to account for changes in background turbulence over the tidal cycle. The wind-driven residual currents are then obtained by subtracting a tide only solution from that due to tide and wind, leaving a wind-driven residual flow (Proctor 1981, 1987; Proctor and Flather 1988; Proctor and Wolf 1989; Davies 1982). A similar approach is used in surge forecasting where a storm surge model is run with a limited number of tidal constituents and meteorological forcing, and the meteorological residual is computed by subtracting a solution derived by running the model with the tide alone. The prediction of total water level at a port is then made by adding the surge residual from the model to a tidal prediction based on a large number of tidal constituents (of order one hundred at a shallow water port) derived from the harmonic analysis of a years data. Similarly the surge at a port is determined from the difference between the observed water level and a tidal elevation prediction based on a summation of tidal constituents (Davies and Flather 1977). The implicit assumption in this linear decomposition is that the tide is not affected by the increased turbulence; both increased bed friction (affecting both elevation and depth-mean currents) and vertical eddy viscosity (affecting tidal current shear)

Corresponding author address: Dr. Alan M. Davies, Bidston Observatory, Proudman Oceanographic Laboratory, Birkenhead, Merseyside L43 7RA, England.

associated with the wind field; and, particularly in shallow water, enhancements in bed friction due to wave–current interaction associated with the surface wind waves. However, the nonlinear nature of the hydrodynamic equations, in particular the parameterization of the vertical eddy viscosity in terms of the flow field, and the quadratic formulation of bottom friction, with a friction coefficient which can be enhanced in shallow water by wave–current interaction (A. G. Davies et al. 1988; A. G. Davies 1986, 1990, 1991; Grant and Madsen 1979, 1986; Christoffersen and Jonsson 1985; Huntley and Bowen 1990; Spaudling and Isaji 1987), suggests that in shallow water the tide, in particular tidal currents, may be changed during major wind events. A consequence of this is that computing a surge residual by subtracting a pure tidal time series from the total record would not be truly valid and would leave tidal energy within the surge residual. Indeed evidence for this has been found in surge residuals computed at shallow water ports using this approach (Amin 1982; Proctor and Flather 1988).

Similarly as short term (of order 30 days) near-bed current measurements are taken in coastal regions (Green et al. 1990) to examine changes in bed stress due to wave–current interaction during major wind events, it is important to know how the near-bed tidal current has been affected during the storm in order to properly interpret and analyze the experimental results.

Since increased bottom friction due to wave–current interaction (Davies and Lawrence 1994) and changes in current profile arising from enhanced levels of turbulence (Aldridge and Davies 1992) have their greatest influence in the near-coastal regime, it is essential to use a high-resolution coastal three-dimensional hydrodynamic model including wave–current interaction effects in order to examine changes in tidal currents.

In this paper a fully three-dimensional model of the eastern Irish Sea (Fig. 1) having a grid resolution of order 1 km, and including wave–current interaction, is used to examine the influence of wind-induced turbulence, and increases in bottom friction due to wave current interaction, upon tidal current profiles in the eastern Irish Sea. A uniform finite-difference grid is used here, although the finite element method (Lynch and Werner 1991; Walters and Werner 1989), with its ability to use finer meshes in the near-coastal region, clearly has some advantages.

The grid of the model, bottom topography, and open boundary input are identical to those used previously (Aldridge and Davies 1993) to compute the M_2 tidal currents in the area. Consequently, any changes in tidal current due to enhanced turbulence of meteorological and wind wave origin can be compared directly with these earlier calculations. Also the model including wave–current interaction has been used to study the wind-induced flow in the region and the influence of wave–current interaction on this flow (Davies and Lawrence 1994).

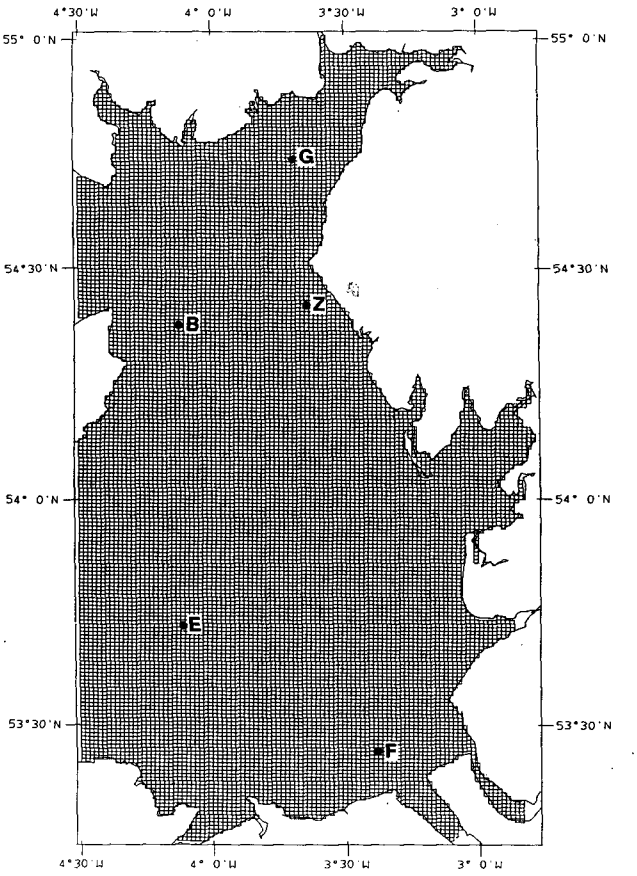

FIG. 1. Finite-difference grid of the model with location of points where current profiles were extracted.

The full three-dimensional model calculations are complemented with a series of more idealized calculations using a single-point model in the vertical. This model can be forced with an oscillatory pressure gradient (at tidal frequency) and an imposed surface wind stress. Calculations with the point model are used to examine in more detail than is possible with the full 3D model (due to the high computational cost of this model) the influence of viscosity parameterization and water depth upon tidal currents. These calculations are used to complement and gain insight into the processes controlling tidal current profiles in the full three-dimensional model.

2. Hydrodynamic models

a. Three-dimensional model

Although stratification effects are important in the Irish Sea, the stratified region is mainly confined to the deep water area (water depth of order 100 m) of low

tidal current strength situated to the west of the Isle of Man (Davies 1993). Also during major wind events when large waves are present, this region becomes well mixed due to wind-induced turbulence. In this paper we are primarily concerned with the eastern Irish Sea where tidal currents are much stronger and the water much shallower (of order 30 m) giving a well-mixed homogeneous region.

To allow for the curvature of the earth, it is necessary to write the three-dimensional hydrodynamic equations in polar coordinates. The full nonlinear three-dimensional equations for a homogeneous region, neglecting the horizontal viscous term, have been presented previously (Davies and Lawrence 1994) and will not be repeated here.

In these equations the coefficient of vertical eddy viscosity μ is related to the flow field using

$$\mu = \alpha(\chi, \phi, t)\Psi(\sigma) \tag{1}$$

with α a constant varying with horizontal position and time and $\Psi(\sigma)$ a fixed profile, with $\sigma = (z + \zeta)/(h + \zeta)$ a normalized vertical coordinate.

Along open boundaries a radiation condition was applied with M_2 tidal elevation and current input as open boundary forcing. Along closed boundaries the normal component of current was set equal to zero.

In the eastern Irish Sea region, depending upon the wind direction and the state of the tide, grid boxes can "flood and dry" over the tidal cycle. The numerical method used to allow for this is identical to that used previously (Aldridge and Davies 1993; Davies and Lawrence 1994) and details will not be repeated here.

For wind-driven flow, the surface stress is set to the externally specified orthogonal components of the wind stress, namely, F_s, G_s; thus

$$-\rho\left(\mu\frac{\partial u}{\partial z}\right)_{-\zeta} = F_s, \quad -\rho\left(\mu\frac{\partial v}{\partial z}\right)_{-\zeta} = G_s \tag{2}$$

with $u(v)$ the eastward (northward) components of the current.

At the seabed, the bed stress components F_B and G_B can be related to the near-bed currents U_h, V_h using a quadratic friction law; thus

$$F_B = \tfrac{1}{2} f_c \rho U_h (U_h^2 + V_h^2)^{1/2},$$

$$G_B = \tfrac{1}{2} f_c \rho V_h (U_h^2 + V_h^2)^{1/2}. \tag{3}$$

In these equations f_c is the current friction factor, given in the absence of wind waves, by

$$f_c = 2C_{100}, \tag{4}$$

where C_{100} is the drag coefficient relating bed stress to currents 100 cm above the seabed, with C_{100} depending upon bed types and forms (Heathershaw 1981). In shallow water where the wind wave orbital velocity is nonzero at the bed, increased levels of turbulence are produced, enhancing the bed stress, and changing the value of f_c and hence the wind-driven flow field (Davies and Lawrence 1994). The inclusion of this effect within the three-dimensional model is considered later in the paper.

b. *Single-point model*

To complement the three-dimensional model, and understand in more detail the importance of viscosity parameterization, water depth, and nonlinear interaction of the wind-driven and tidally forced flow through the viscosity term, a single-point model was also used, of the form

$$\frac{\partial u}{\partial t} - \gamma v = \frac{\partial P}{\partial x} + \frac{\partial}{\partial z}\left(\mu\frac{\partial u}{\partial z}\right) \tag{5}$$

and

$$\frac{\partial v}{\partial t} + \gamma u = \frac{\partial P}{\partial y} + \frac{\partial}{\partial z}\left(\mu\frac{\partial v}{\partial z}\right). \tag{6}$$

In these equations, γ is a fixed Coriolis parameter with pressure gradient terms $\partial P/\partial x$ and $\partial P/\partial y$ given by

$$\frac{\partial P}{\partial x} = h_x\omega\cos(\omega t + g_x),$$

$$\frac{\partial P}{\partial y} = h_y\omega\cos(\omega t + g_y) \tag{7}$$

with h_x and h_y specified amplitudes and g_x, g_y phases of sinusoidal forcing at a frequency ω.

Equations (5) and (6) were also solved subject to identical boundary conditions, namely, specified external wind components F_s, G_s [Eq. (2)] and quadratic friction at the bed [Eq. (3)]. However, in order to remove the nonlinearity associated with the quadratic friction term, leaving a linear system in the case of a time invariant μ, an alternative bottom boundary condition, namely, a no-slip condition, $u = v = 0$, was considered at the seabed in the single-point model.

3. Numerical solution and formulation of the vertical eddy viscosity

a. *Numerical solution*

The hydrodynamic equations are solved using the Galerkin/spectral method in the vertical, in terms of an expansion of basis functions $f_r(\sigma)$ (modes), yielding a continuous current profile from sea surface to seabed. Extensive details of the solution of the hydrodynamic equations using this approach can be found in Davies (1986, 1987, 1991) and will not be repeated here.

The choice of basis set functions $f_r(\sigma)$ is, in theory, arbitrary; however, there are major computational advantages (Davies and Stephens 1983) in choosing them to be eigenfunctions of the eddy viscosity profile, subject to a slip or no-slip condition. A highly computationally efficient time-splitting algorithm (Davies 1987; Aldridge and Davies 1993) is used to integrate the three-dimensional hydrodynamic equations in time.

b. *Eddy viscosity formulation*

In the series of calculations described later a number of eddy viscosity formulations are presented. The simplest is a constant coefficient of eddy viscosity that does not vary in the vertical (profile A, Fig. 2). An alternative formulation based upon observations (Bowden et al. 1959; Bowden 1978; Bowden and Ferguson 1980) is a linear decrease in the near-bed layer from a value μ_1 to μ_0 over a height $h_1 = \beta h$, with β a coefficient of order 0.1 to 0.2 representing a decrease in turbulence in the near-bed region (profile B, Fig. 2). By analogy with the near-bed layer, a linear decrease may be expected in the near-surface layer over a distance $h_2 = \beta h$ (profile C, Fig. 2). However, in the case of wind-driven flow increased turbulence associated with wave breaking might be expected at the surface, leading to profile D in Fig. 2.

Based upon Irish Sea observations (Bowden et al. 1959; Bowden 1978; Wolf 1980) and also results from a turbulence energy model (Davies 1991), an appropriate simple parameterization of eddy viscosity magnitude α is of the form

$$\alpha = k_2(\bar{u}^2 + \bar{v}^2)h \tag{8}$$

with k_2 of order 2.5×10^{-3} and h water depth.

An alternative parameterization (Davies and Aldridge 1993) is

$$\alpha = k_3\bar{U}^2/S_1 \tag{9}$$

with $\bar{U}$ depth-mean current magnitude, $S_1 = 1.0 \times 10^{-4}\ \mathrm{s}^{-1}$ a characteristic frequency, and $k_3 = 0.2$ a dimensionless coefficient.

Eddy viscosity is then given by Eq. (1) with

$$\Psi(\sigma) = \frac{\psi(\sigma)}{\int_1^0 \psi(\sigma)}\, d\sigma, \tag{10}$$

where $\Psi(\sigma)$ is a normalized viscosity profile derived from the viscosity profiles $\psi(\sigma)$ given in Fig. 2.

4. Representation of wave–current interaction

The wave–current interaction model of Grant and Madsen (1979) in the form published by Signell et al. (1990) was used in the models to parameterize increased turbulence due to wave effects by changes in the wave friction coefficient f_c. The effect of enhanced bed turbulence when wind wave effects are present influences the flow field computed by the hydrodynamic model through an increase in the current friction factor f_c and hence the bed stress in the hydrodynamic model. Here only the major steps in the formulation of the wave–current interaction model for colinear flow are described (Signell et al. 1990), although further details can be found in Grant and Madsen (1979).

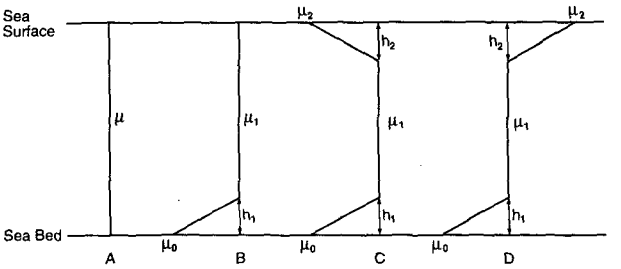

FIG. 2. Schematic of the various eddy viscosity profiles used in the calculations.

For a colinear flow, the total bed shear stress τ_T based upon an instantaneous current shear stress τ_c and maximum wave bed stress τ_w is given by

$$\tau_T = \tau_c + \tau_w \tag{11}$$

with

$$\tau_w = \tfrac{1}{2} f_w \rho U_0^2, \tag{12}$$

where U_0 is the maximum near-bed wave orbital velocity, and f_w is the wave friction factor.

The near-bed wave orbital velocity is given by

$$U_0 = \frac{a_w \omega}{\sinh kh} \tag{13}$$

with a_w wave amplitude, ω wave frequency, and k wavenumber determined from the linear dispersion relation

$$\omega^2 = (gk)\tanh(kh), \tag{14}$$

where g is acceleration due to gravity.

The wave friction factor f_w can be readily computed from the semiempirical expression of Jonsson (1967) and Jonsson and Carlsen (1976) based upon laboratory observations; namely,

$$\frac{1}{4\sqrt{f_w}} + \log_{10}\left(\frac{1}{4\sqrt{f_w}}\right) = -0.08 + \log_{10}\left(\frac{A_b}{k_b}\right), \tag{15}$$

where $k_b = 30z_0$, z_0 is the roughness length and $A_b = U_0/\omega$.

Here, for computational efficiency, we assume that the current does not influence the wave field. (A consistent assumption with the method in which the hy-

drodynamic model is run, whereby the wave field is supplied externally and hence there is no dynamic feedback from the current model.) The current bed stress τ_c is influenced by the wave field, and this influences the computed flow field. In calculations in which the viscosity is determined by the total flow field, a nonlinear interaction occurs between wind wave effects, wind-driven flow, and tidal flow.

The calculation of an effective drag coefficient f_c taking into account wave effects proceeds as in Signell et al. (1990). Since the present model assumes that the current does not influence the wave field, then the wave friction velocity is given by

$$U_{*w} = \left(\frac{\tau_w}{\rho}\right)^{1/2} \tag{16}$$

with τ_w given by (12) and f_w taken from (15).

At time $t = 0$, an initial current friction factor f_c excluding wind wave turbulence was determined from

$$f_c = 2\left[\frac{K}{\ln(30z_r/k_{bc})}\right]^2 \tag{17}$$

with k_{bc} taken as the Nikuradse roughness $k_b = 30z_0$, $K = 0.4$ von Kármán's constant, and z_r the reference height at which the slip condition is applied. In the calculations considered here, this was taken as 100 cm above the bed.

Having determined f_c, U_{*c} can be readily computed from

$$U_{*c} = \left(\frac{\tau_c}{\rho}\right)^{1/2} \tag{18}$$

with τ_c the vector sum of F_B, G_B from Eq. (3).

The combined friction velocity U_{*cw} for waves and currents is given by

$$U_{*cw} = (U_{*c}^2 + U_{*w}^2)^{1/2}. \tag{19}$$

The apparent bottom roughness k_{bc} felt by the current due to the presence of the waves is given by

$$k_{bc} = k_b\left[C_1 \frac{U_{*cw}}{U_w}\frac{A_b}{k_b}\right]^{\beta} \tag{20}$$

with $C_1 = 24.0$ (Grant and Madsen 1979) and

$$\beta = 1 - \frac{U_{*c}}{U_{*cw}}. \tag{21}$$

This value of k_{bc} is then used at the next time step to determine f_c and hence the bed stress in the three-dimensional model using Eq. (3).

5. Numerical calculations

a. Eastern Irish Sea region

Water depths in the area decrease from the order of 50 m close to the model's western boundary (Fig. 3)

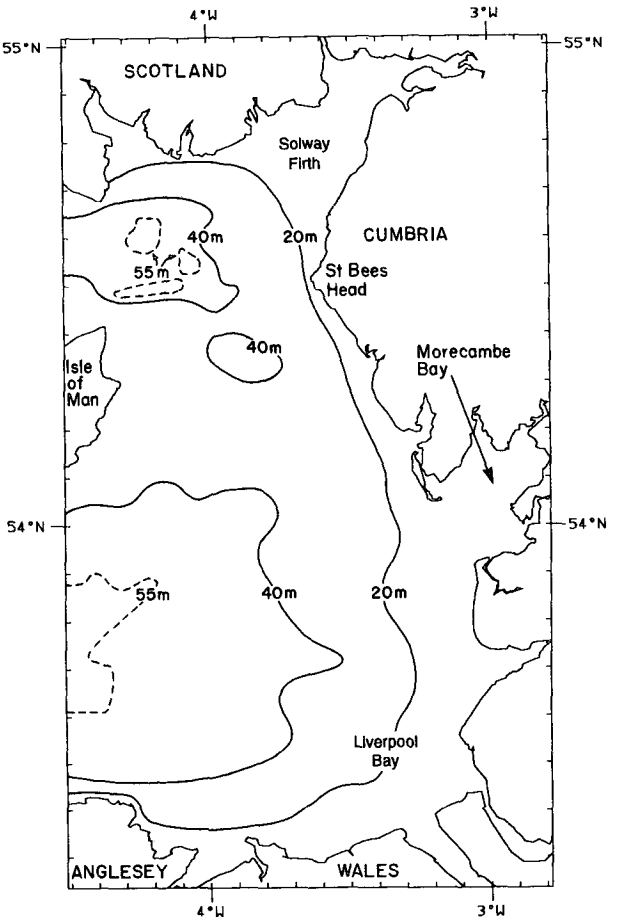

FIG. 3. Contours (in meters) of the bottom topography of the eastern Irish Sea.

to depths less than 20 m, in a shallow near-coastal band, with "wetting and drying" alternating at different phases of the tide in the near-coastal region. A number of bed types from mud through sand to gravel are found in the region, with a muddy area located near St. Bees Head and to the south of it. The sand region is concentrated in the southern part of the modeled area, with gravel situated in the western part of the region. A detailed distribution of bed types is given in Aldridge and Davies (1993) and Davies and Lawrence (1994). Also, there are a substantial number of bed forms in the Irish Sea that cannot be resolved on a 1-km grid. The influence of these bed forms upon turbulence energy intensity, and hence tidal dissipation, can only be included in the present model by regarding the bed roughness length z_0 as an effective roughness length taking account of energy loss by form drag and skin friction. Since the level of wave–current interaction [Eq. (20)] depends upon the bed roughness length z_0 and intensity of near-bed current, it is essential to use a sufficiently fine grid (Fig. 1) to resolve the various

TABLE 1. Summary of calculations performed with the eastern Irish Sea model.

Calculation	Tidal forcing	Wind stress		Wave field		Wave friction f_w	Z_0 $k = f_c/2$
		F_s	G_s	H_s	T_M		
1	yes	0.0	0.0	0.0	0.0	0.0	0.00375
2	yes	0.0	1.0	0.0	0.0	0.0	0.00375
3	yes	0.0	1.0	1.0	10.0	0.045	0.00375
4	yes	0.0	1.0	1.0	10.0	0.045	Bed type
5	yes	0.0	1.0	3.0	10.0	Eq. (30)	Bed type

bed types and spatial variability of the bed currents and hence the bed stress.

b. M_2 tidal elevations, currents, and wind-driven currents

In an initial calculation (calculation 1, Table 1) the model was integrated forward in time from a state of rest with M_2 tidal forcing identical to that used by Aldridge and Davies (1993) applied along the open boundary. Eddy viscosity was parameterized using Eq. (8) with $k_2 = 0.0025$, and a bottom friction coefficient $k = f_c/2 = 0.00375$, a value which yielded an accurate tidal solution in the area (Aldridge and Davies 1993).

After four tidal cycles, a sinusoidal tidal solution was obtained. The elevation and flow field from the fifth tidal cycle were harmonically analyzed yielding the cotidal chart shown in Figs. 4a,b. Profiles of the amplitude of the u and v component of the M_2 tidal current at selected points (Fig. 1) are shown in Fig. 5.

Tidal elevation and current amplitude were identical to those computed by Aldridge and Davies (1993) and

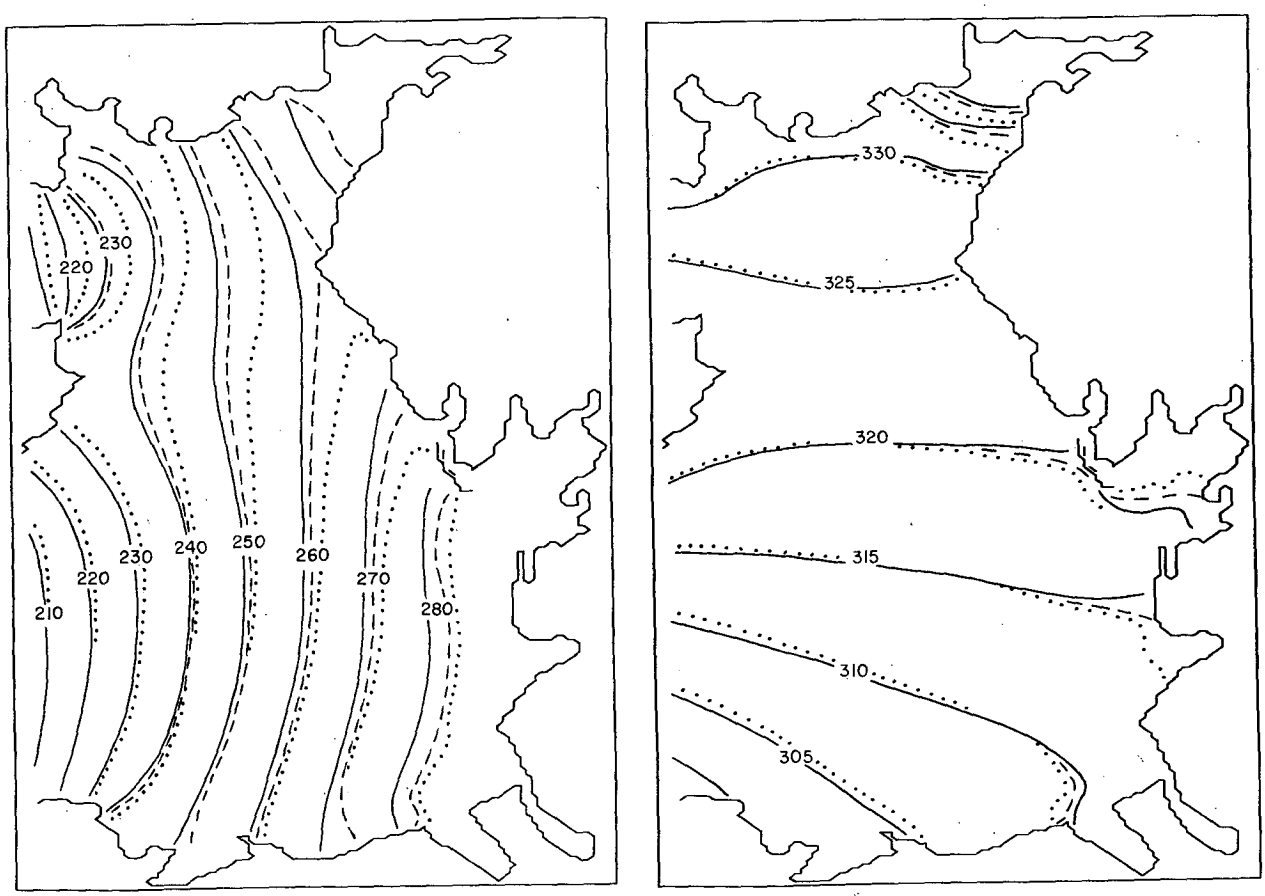

FIG. 4. (a) Computed M_2 coamplitude chart determined with M_2 only (solid), M_2 tide and a westerly wind stress of 1 N m^2 (dashed), and M_2 tide with a wind stress and wave–current interaction (H_s = 3.0 m, T_M = 10 s) (dotted). (b) As in (a) but for phase.

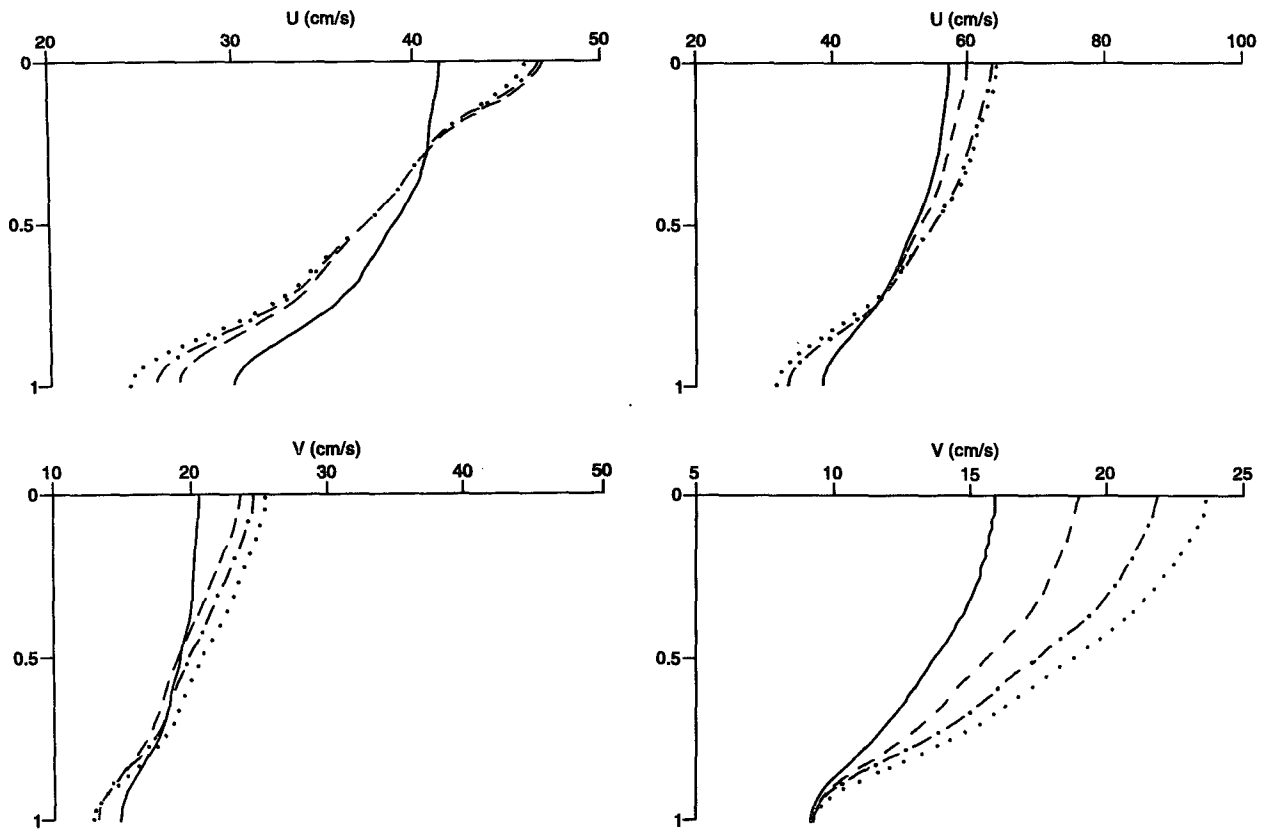

FIG. 5. Profiles of the amplitude of the u and v components of the M_2 tide at locations B (left) and F (right) (see Fig. 1) computed with tidal forcing only (solid), tidal forcing and a westerly wind stress (dashed) tidal and wind forcing with wave–current interaction (H_s = 1.0 m, T_M = 10 s) (dot-dashed); and with wave–current interaction (H_s = 3.0 m, T_M = 10 s) (dotted).

were found to be in good agreement with observations (see tables of statistics in Aldridge and Davies 1993). The coamplitude chart (Fig. 4a) shows a uniform increase in tidal amplitude as the tide propagates from deep water into the shallow coastal regions. Similarly, the phase of the tide increases uniformly from south to north (Fig. 4b).

Profiles of the u and v components of the M_2 tidal amplitude at a number of points (B, E, F, G, Z) in water depths ranging from the order of 50 m (B, E) to much shallower (h = 10 m) near-coastal (F, G, Z) exhibit an almost shear-free layer in the upper part of the water column with a frictionally retarded bottom boundary layer in which current velocities decrease more rapidly. In deep water (position B, E) tidal current profiles are similar to those shown at position B (Fig. 5), with shallow water profiles (position F, G, Z) characterized by position F (Fig. 5).

As we will show later, in order to understand changes in M_2 tidal current profile and the M_2 cotidal chart, due to the influence of meteorological forcing and the enhancement of bed stress caused by wave–current interaction, it is necessary to know the spatial distribution of the M_2 tidal currents, in particular the bed currents since these are important in determining the bed stress and hence energy dissipation.

The major and minor axes of the M_2 current ellipse at the seabed at every third grid point are given in Fig. 5 in Aldridge and Davies (1993). Referring to their figure, it is evident that a region of low tidal current (major axis of order 10 cm s^{-1}) exists to the east of the Isle of Man, with tidal currents increasing moving eastward toward the English coast with a subsequent decrease in the near-coastal regime. Tidal currents also increase in strength going northward toward the Solway Firth, although they are significantly lower (of order 50 cm s^{-1}) than those in the region to the southeast of the Isle of Man (currents of order 100 cm s^{-1}).

In a subsequent calculation (calculation 2, Table 1) identical tidal input was used along the model's open boundary, but a spatially uniform wind stress of 1.0 N m^{-2} corresponding to a uniform westerly wind was also applied. Again after four tidal cycles a sinusoidal solution was obtained, with the fifth harmonically analyzed for the amplitude and phase of the surface elevation and tidal current profiles and residual flows at a selected number of points (Fig. 1).

TABLE 2. Values of U_0 (cm s^{-1}) [(a) for a wave amplitude 0.5 m, (b) for a wave amplitude 1.5 m] and wave friction factor f_w for a range of water depths h (m) and bed roughness lengths Z_0 (cm) with corresponding $C_{100} = f_c/2$ values, for a wave amplitude of 1.5 m and period of 10 s.

			Bed type			
			Model average	Mud	Gravel	Rippled sand
			Z_0 (cm)			
			0.146	0.02	0.3	0.6
	U_0 (cm s^{-1})		C_{100}			
h (m)	(a)	(b)	0.00375	0.0022	0.0047	0.0061
10	42.8	128.4	0.0303	0.0138	0.0433	0.0660
20	25.5	76.5	0.0391	0.0166	0.0571	>0.07
30	17.0	51.0	0.0480	0.0194	>0.07	>0.07
40	11.7	35.0	0.0626	0.0225	>0.07	>0.07
50	8.0	24.0	>0.07	0.0264	>0.07	>0.07

It is evident from Figs. 4a,b that the inclusion of the wind-driven flow has changed the distribution of coamplitude and cophase lines, particularly in the nearshore region (note the shift in position of the 270-cm and 280-cm coamplitude lines), corresponding to a reduction in tidal amplitude by the order of 5 cm. The reason for this change in tidal amplitude in the nearshore region is that wind-induced currents in these regions are stronger (Davies and Lawrence 1994) than in the offshore areas due to the shallower water depth. A consequence of this is that since the bed stress is determined through the quadratic law, it is enhanced by the presence of the additional wind-driven flow; hence, frictional dissipation increases, thus reducing tidal amplitudes.

In offshore regions (excluding the shallow Solway Estuary) (Fig. 4a), the most significant changes in the position of the coamplitude lines occurs in the northern rather than the southern part of the region. Since water depths in both these areas are comparable, this cannot be attributed to variations in bottom topography. Again the reason for this is that tidal current strength is significantly weaker in the northern rather than the southern part of the eastern Irish Sea. Consequently the addition of a wind-driven flow has a larger effect upon tides in the north than those in the south. Besides the influence of the wind-driven flow upon the bed stress, changes in the flow also influence the magnitude of the eddy viscosity, which is related to the intensity of the depth-mean current [Eq. (8)]. Consequently, in a region of rectilinear tidal flow in the absence of wind-driven flow the eddy viscosity reaches a maximum twice within the tidal cycle at times of maximum tidal velocity. At times when the eddy viscosity is a maximum, the wind's energy can diffuse to greater depths than at times when the eddy viscosity is at a minimum, when the wind's energy can only penetrate the surface layer, giving larger surface currents (Dyke 1977). In a region in which the tidal current ellipse is circular, then in the absence of a wind-driven flow, eddy viscosity is constant (Davies 1990), and higher harmonics can only be generated by the other nonlinear mechanisms in the model, for example, the advective terms and quadratic bottom friction. We might therefore expect differences in coupling between tidal and wind-induced currents in different regions depending upon the nature of the tidal current ellipse. As we will show later, a consequence of a time-varying eddy viscosity related to the tidal flow and an externally applied wind stress is that some of the wind's energy can appear in the tidal signal at both the fundamental and higher harmonics, depending upon the alignment of the wind and tidal current ellipse. A more detailed explanation of this is given in the next section in connection with the point model.

An increase in near-surface M_2 tidal current, particularly at point B (Fig. 5), occurs when the wind forcing is included. The M_2 tidal current at depth, however, is often reduced (Fig. 5) when wind effects are included due to increases in bed frictional effects. In contrast at points B, E, and F (see Fig. 1 for location of points), the inclusion of the wind forcing increases the M_2 surface tidal current by the order of 5 cm s^{-1} (an increase of more than 10% at site B).

In a subsequent calculation (calculation 3, Table 1), identical tidal and wind forcing were used with the inclusion of wave–current interaction, due to a wave field in the wind direction having a wave amplitude a_w = 0.5 m (significant wave height H_s = 1.0 m) and wave period T_M = 10 s, with f_w fixed at 0.045. Since the wave orbital velocity of wind waves decreases rapidly with depth below the sea surface, then in deep water (water depths of order 50 m) the bed orbital velocity was small (of order 8 cm s^{-1}) (Table 2) and the current friction factor f_c was not enhanced by wave–current interaction. In slightly shallower water (water depths of order 30 m), f_c was enhanced, leading to a slight reduction in the u component of near-bed tidal current (Fig. 5, point

B). At location E, a reduction in the magnitude of the v component of tidal current throughout the whole water column occurred, whereas at location B, the magnitude of the v component increased slightly. In very shallow water (water depths of order 20 m) the near-bed wave orbital velocity is of order 26 cm s^{-1}, and the current friction factor is increased significantly [by a factor of 2.5 (Davies and Lawrence 1993)] producing a decrease in the near-bed u component of the tidal current (e.g., Fig. 5, point F), although the surface tidal current increases. Aldridge and Davies (1993) found a similar change in the u tidal current profile with increasing friction coefficient in a tidal model of the eastern Irish Sea. They found that when k was increased by a factor of two, the near-bed tidal velocity decreased due to the enhanced bed stress, but the surface tidal velocity increased to give the same depth-mean current. Obviously, an identical effect occurs here when the value of k is increased as a result of wave–current interaction.

The near-bed wind-driven residual flow in deep regions is reduced slightly by wave–current interaction (waves with H_s = 1.0 m, T_M = 10.0 s) in areas where the tidal current is weak (Fig. 6, position B); however, in comparable water depths (position E) where the tidal current is stronger it is not changed significantly. In shallow water regions where the near-bed wave orbital velocity is significant, but tidal currents are strong (Fig. 6, position F), the u component of the residual flow (the component in the wind direction) is not changed, with the v component reduced at all water depths. The differences in response of the u and v component of current, at position F, close to the coast (Fig. 1) can be readily explained. In the case of the u component, the flow is directly wind forced and is not significantly influenced by wave–current interaction. The northerly v component of current, however, is essentially pressure driven (though modified by frictional and rotational effects) by the build up of surface elevation against the coast (Fig. 7). Including wave–current interaction increased bottom friction, thus reducing this pressure gradient (Davies and Lawrence 1994) and hence reducing the northerly flow at all depths.

In this series of calculations a constant bed roughness ($z_0 = 0.146 \times 10^{-2}$ m) compatible with a k value of 0.00375 was used throughout. In practice there are a number of bed types over the region, and to account for this the above calculation was repeated (calculation

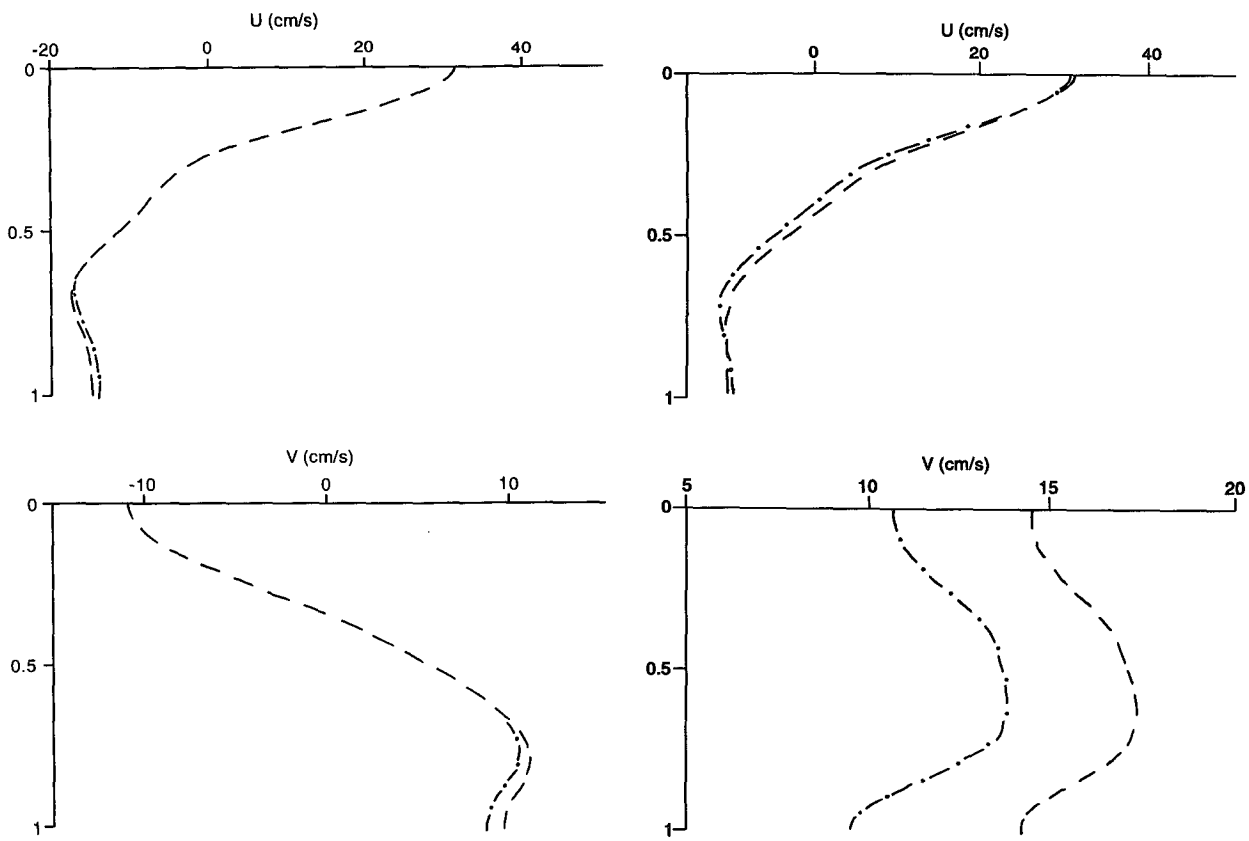

FIG. 6. Profiles of the u and v components of the wind-induced currents at points B (left) and F (right) computed with a westerly wind stress (dashed) and a westerly wind stress with wave effects (H_s = 1.0 m, T_M = 10.0 s) (dot-dashed).

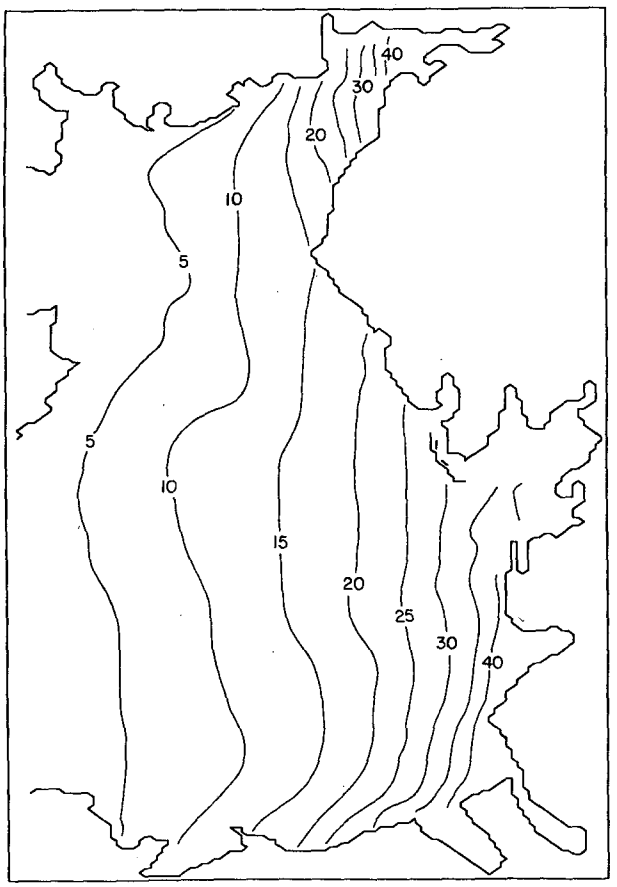

FIG. 7. Residual sea surface elevation contours (m) due to a westerly wind stress of 1 N m^{-2}.

4) with a varying z_0, including these bed types. Consequently, a spatially varying wave–current interaction effect, reflecting both the variations in water depth and bed types, now influenced the flow field. However, computed M_2 tidal and residual current profiles at the various locations were only slightly different (of order a few centimeters per second) from those computed previously. The reason for this is that the major differences from one location to another arise primarily from variations in water depth and its influence upon wave orbital velocity and hence wave–current interaction rather than z_0. Also in this calculation f_w was held constant (Table 1).

In practice, variations in water depth and roughness length z_0 will lead to a spatial variation in the wave friction factor f_w (Table 2), which will significantly influence the wave bed stress and hence wave–current interaction. In a final calculation (calculation 5, Table 1) both a varying bottom roughness z_0 and a value of f_w determined from Eq. (30) were used in the model. Since including these effects improves the physical realism of the model, the wave amplitude (a_w) was increased to 1.5 m (H_s = 3.0 m), a physically more realistic value for the wind stress conditions considered here; namely, those occurring during major storm events (Davies and Jones 1992b; Carter 1982; Draper 1992). Also during these major storm events, swell produced in the Atlantic Ocean can propagate into the Irish Sea. Since swell waves have a long period, they will enhance the bed stress in much deeper water depths than wind waves generated locally in the area.

Changes in the position of the M_2 coamplitude lines (Fig. 4a) due to increased turbulence associated with the wind-driven flow and enhanced wave–current interaction are clearly evident, reducing the M_2 tidal elevation amplitude by the order of 10 cm in shallow near-coastal regions. Part of this reduction in amplitude comes from increased frictional effects produced by the wind-driven currents, and partly from increases in the drag coefficient due to the wind wave turbulent boundary layer at the seabed.

The significantly larger change in the position of the coamplitude and cophase lines in shallow water (Figs. 4a,b), which occurs in calculation 5, is due to the enhanced level of friction in shallow water arising from the larger wave amplitude. Similarly the M_2 tidal current profile computed with this enhanced level of wave–current interaction exhibits a reduction in near-bed tidal currents (Fig. 5, points B and F) due to the increase in bed friction, although a slight increase in the surface M_2 tidal current occurs in these positions. However, in very shallow water (point G, Fig. 1) the computed M_2 tidal current profile showed a marked decrease at all depths. In this very shallow water region, Davies and Lawrence (1994) found that the value of C_{100} was increased by a factor of over five due to wave–current interaction when a_w = 1.5 m, T_m = 10 s; this is the reason for the marked reduction in M_2 tidal currents at all depths. Although this effect will occur in nature, it is unusual to have such large waves in these shallow water regions. [Draper (1992) does, however, report waves of this order in Morecambe Bay.]

In very near coastal locations (e.g., point Z, Fig. 1), the profile of the amplitude of the u and v components of the M_2 tidal current changed very significantly, showing a reduction in magnitude of the surface tidal current. The reason for this will be discussed in more detail in the section concerned with the point model (see later).

c. *Higher tidal harmonics*

In the previous section we have examined the influence of enhanced levels of friction and turbulence of meteorological and wind wave origin upon the wind-driven residual flow, and M_2 tidal elevation and current.

The nonlinear terms, namely, the advective terms and quadratic bottom friction term in the hydrodynamic equations, can transfer energy at the M_2 fre-

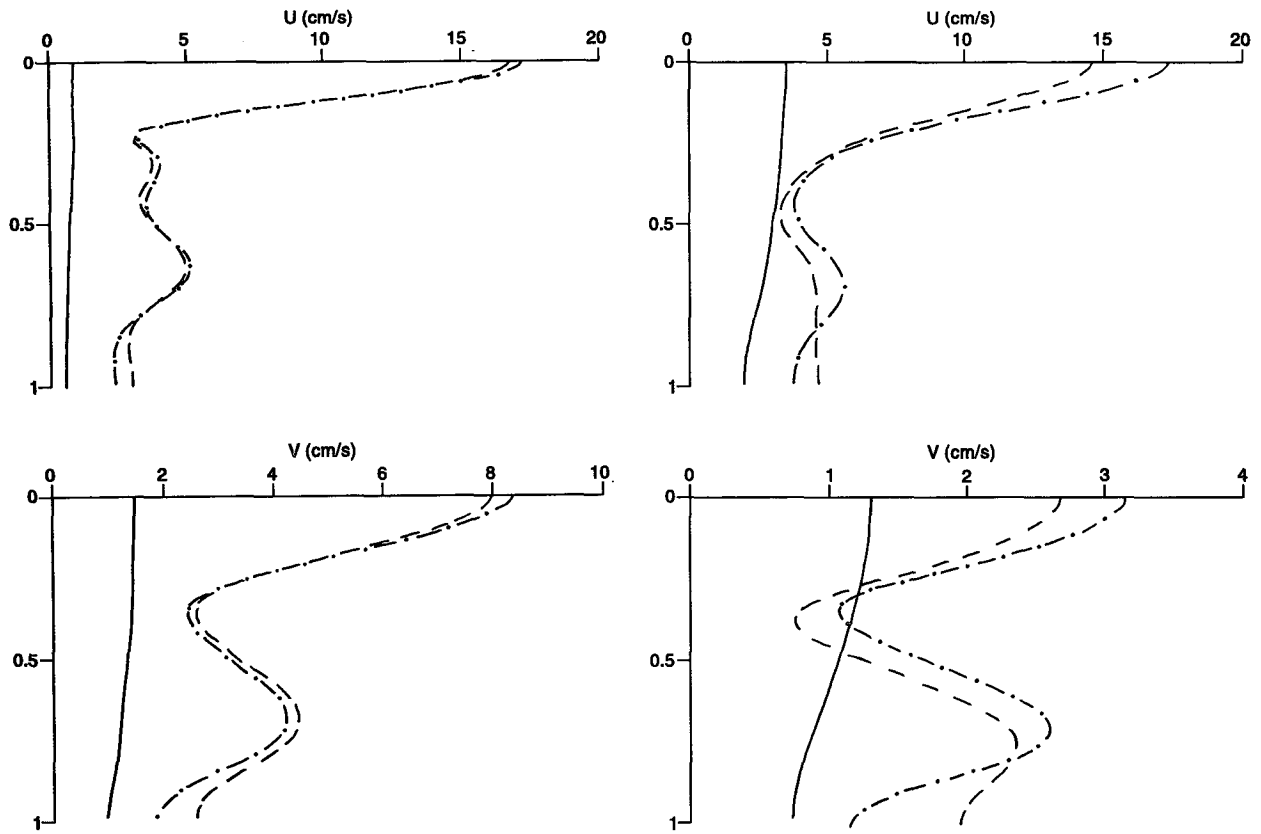

FIG. 8a. Profiles of the amplitude of the u and v components of the M_4 tide at locations B (left) and F (right) in the Irish Sea (see Fig. 1) computed with M_2 tidal forcing only (solid), tidal forcing and a westerly wind stress (dashed), and tidal forcing, westerly wind stress, and wave–current interaction (H_s = 1.5 m, T_M = 10.0 s) (dot-dashed).

quency to the higher harmonics, that is, M_4 (principally through the advective terms) and M_6 (principally through the bottom friction term) and also to a small residual flow [current magnitude of order 5 cm s^{-1} in the eastern Irish Sea, Aldridge and Davies (1992)], which is the tidal residual. The generation of the higher harmonics by these mechanisms is well known and the M_4 tidal production on the shelf using a full nonlinear three-dimensional hydrodynamic model was simulated some time ago (Davies 1986).

However, as we shall demonstrate, other important nonlinear mechanisms exist, when the eddy viscosity depends upon the total flow field (tidal plus wind), which can transfer energy from the wind-driven flow into the tidal flow, both at the fundamental and its higher harmonics. To examine the importance of the flow dependence of the eddy viscosity in generating higher harmonics, it is advantageous to omit the nonlinear advective terms in the hydrodynamic equations, thereby removing an M_4 generation mechanism. As shown by Aldridge and Davies (1993) omission of these terms has a negligible influence on the M_2 tidal currents, and hence upon the background level of turbulence.

Vertical profiles of the amplitude of the u and v components of the M_4 tidal current at positions B, E, F, G, and Z (Fig. 1), computed with the tide alone, show a small M_4 signal (as expected in the absence of the advective terms), with magnitude decreasing slightly from sea surface to seabed (see profiles at positions B and F in Fig. 8a). However, M_4 tidal current profiles extracted by harmonic analysis of model output determined with both meteorological and tidal forcing (calculation 2) are much higher in the near surface (u-current amplitude of order 15 cm s^{-1}, v-current amplitude of order 7 cm s^{-1}, points B, E), although amplitude decreases with depth (Fig. 8a).

Profiles of M_4 tidal currents computed with meteorological forcing and wave–current interaction included in deep water (positions B and E) are not significantly different from those computed without wave–current interaction (in fact no difference was found at E) (see the profile at position B in Fig. 8a). However, in shallow water, position F, the components

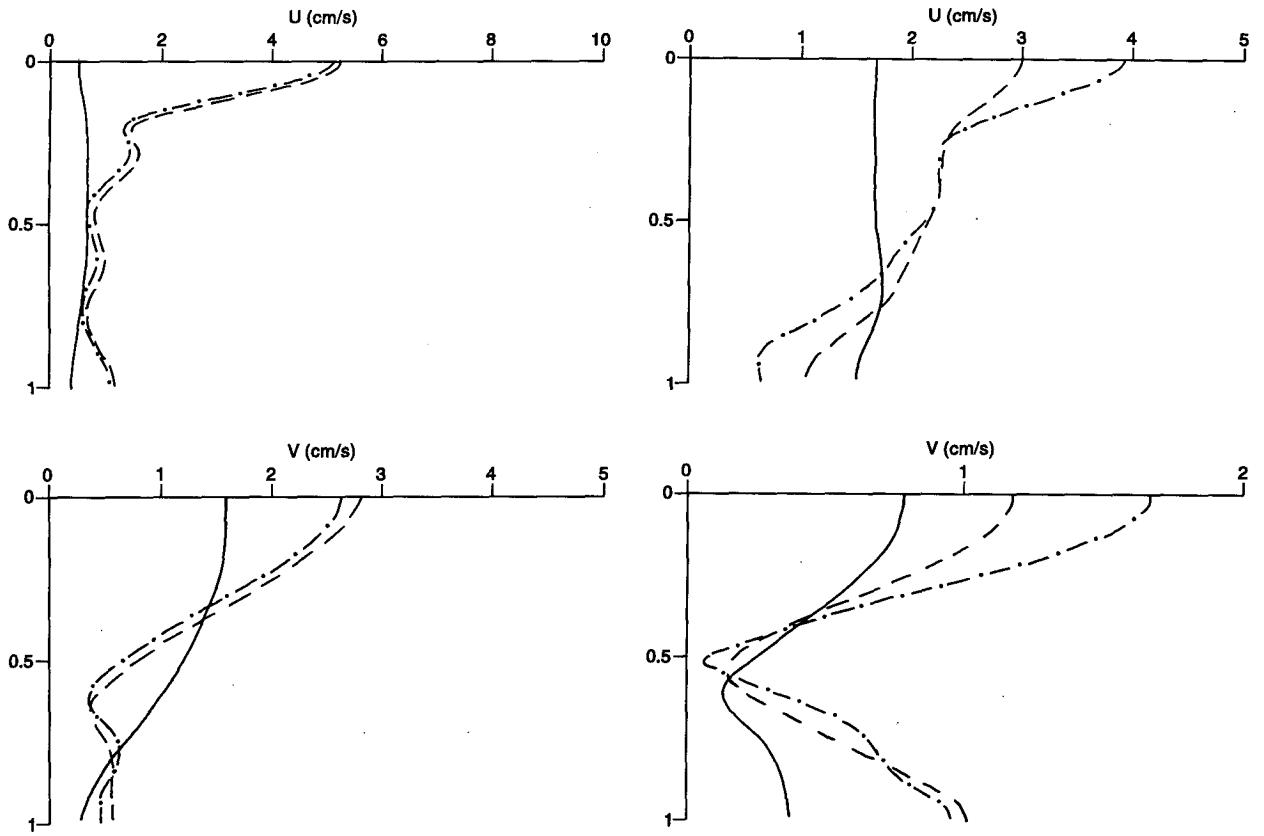

FIG. 8b. As in Fig. 8a but for the M_6 component of current at points B and F.

of the M_4 tidal current increase slightly at the surface when wave–current interaction is included (Fig. 8a), with a reduction at the bed due to increased friction.

This source of M_4 tidal energy is obviously associated with the wind field and time variations of the eddy viscosity, which determine the rate at which the wind's energy can diffuse to depth. To examine this further, M_4 tidal current profiles in very shallow water (positions G and Z) were determined from calculation 5, $H_s = 3.0$ m, $T_M = 10.0$ s. These current profiles showed that in these very shallow regions the u component (the component in the wind direction) of the M_4 tide is significantly increased. A detailed discussion of these processes will be presented later in connection with a point model.

Besides enhancing the magnitude of the M_4 tidal current, a time-varying eddy viscosity related to the tidal flow should also increase the magnitude of the other higher harmonics, in particular M_6. A slight increase, again primarily in the near-surface region when wind forcing is included, is clearly evident (Fig. 8b). Again, the inclusion of wave–current interaction effects has a negligible influence in deep regions (at location E there was no effect), although in shallow water (position F) it increases the surface u component of the M_6 current and decreases its value at the bed (Fig. 8b). For the v component the change appears to be more complex with an increase at both surface and bed. A more detailed discussion of the mechanisms producing these results will be considered in connection with the point model.

6. Idealized single-point model calculations

To complement, and gain a better understanding of the mechanisms influencing the coupling of tidal and wind-driven flows, it is necessary to perform a series of calculations using the single-point model in the vertical [Eqs. (5) and (6)]. To examine in detail the influence of the nonlinear term produced by a time-varying eddy viscosity, it is necessary to remove the other nonlinear term (i.e., quadratic bottom friction) when solving Eqs. (5) and (6). To this end, the equations were solved subject to the no-slip bottom boundary condition.

Since a no-slip bottom boundary condition was used, a linear decrease in viscosity in the near-bed region (profile B, Fig. 2) was applied with a $\mu_0:\mu_1$ ratio of 0.0001 to 0.1 and β set at 0.2; physically realistic values (Davies 1993) in a model using a no-slip bottom boundary con-

TABLE 3. Summary of calculations performed with the single-point model, of tidal and wind-driven flow.

Calculation	h_x	h_y	g_x	g_y	Type	F_s	G_s	Viscosity Profile	h (m)
1	1.0	1.0	0.0	90.0	Circular	1.0	0.0	B	10
2	1.0	1.0	0.0	90.0	Circular	1.0	0.0	C	10
3	1.0	1.0	0.0	90.0	Circular	1.0	0.0	D	10
4	1.0	1.0	0.0	90.0	Circular	0.5	0.0	B	10
5	1.0	0.0	0.0	0.0	Rectilinear	0.0	0.0	B	10
6	1.0	0.0	0.0	0.0	Rectilinear	1.0	0.0	B	10
7	1.0	0.0	0.0	0.0	Rectilinear	0.5	0.0	B	10
8	1.0	0.0	0.0	0.0	Rectilinear	0.0	−0.5	B	10
9	1.0	0.0	0.0	0.0	Rectilinear	1.0	0.0	B	30

dition. Also, in order to understand the coupling of the u and v components of current produced by a flow-dependent time-varying viscosity [Eq. (8), with $k_2 = 2.5 \times 10^{-3}$], the influence of coupling due to rotation was also removed (i.e., $\gamma = 0.0$ in all calculations).

In an initial series of calculations, coupling between a wind-driven flow and a tidal flow with $\omega = 30°\ h^{-1}$, a semidiurnal tide denoted D_2, characterized by a circular tidal current ellipse in shallow water $h = 10$ m, was examined (Table 3). This problem is considered first because with a circular tidal ellipse, the orientation of the wind direction with respect to the major axis of the ellipse is not relevant. Also, as shown previously (Davies 1990), a flow-dependent eddy viscosity produced by a circular tidal current ellipse is constant in time; hence, any time variation is produced by the wind-driven flow. By setting $h_x = h_y = 1.0$ m s^{-1}, $g_x = 0.0$, and $g_y = 90.0°$ (calculation 1, Table 3) in Eq. (7) a circular tidal ellipse was produced with eddy viscosity magnitude depending upon the flow field [Eq. (8)], but remaining constant in time.

The effect of imposing wind forcing in the x direction, produced by imposing a wind stress $F_s = 1.0$ N m^{-2}, $G_s = 0.0$ at time $t = 0$, is to produce an additional wind-driven flow in the x direction, a consequence of which is that the total flow, tidal plus wind, is no longer constant in time and hence produces a time-varying eddy viscosity (Figs. 9a–c). The magnitude of the wind-induced flow in this case ($F_s = 1.0$ N m^{-2}, $G_s = 0.0$) is such that the total flow (wind plus

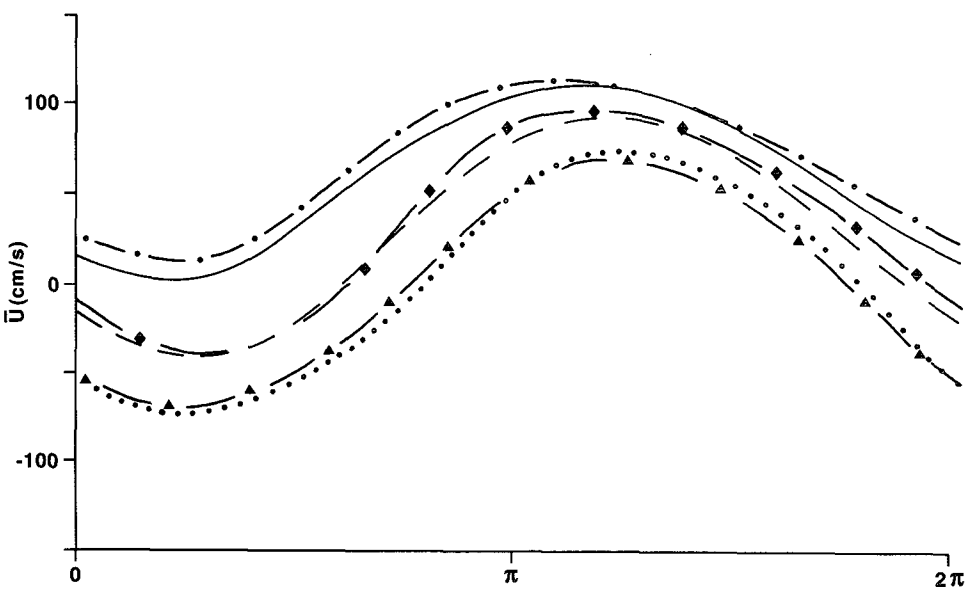

FIG. 9a. Time series over one tidal cycle of the depth-mean u component of current in a water depth $h = 10$ m, computed for (i) circular tidal current ellipse with $F_s = 1.0$ N m^{-2}, $G_s = 0.0$ (calculation 1) (solid); (ii) circular tidal current ellipse with $F_s = 0.5$ N m^{-2}, $G_s = 0.0$ (calculation 2) (dashed); (iii) rectilinear tide (calculation 5) (dotted); (iv) rectilinear tide with $F_s = 1.0$ N m^{-2}, $G_s = 0.0$ (calculation 6) (dot-dashed); (v) rectilinear tide with $F_s = 0.5$ N m^{-2}, $G_s = 0.0$ (calculation 7) (diamonds); and (vi) rectilinear tide with $F_s = 0.0$, $G_s = -0.5$ N m^{-2} (calculation 8) (triangles).

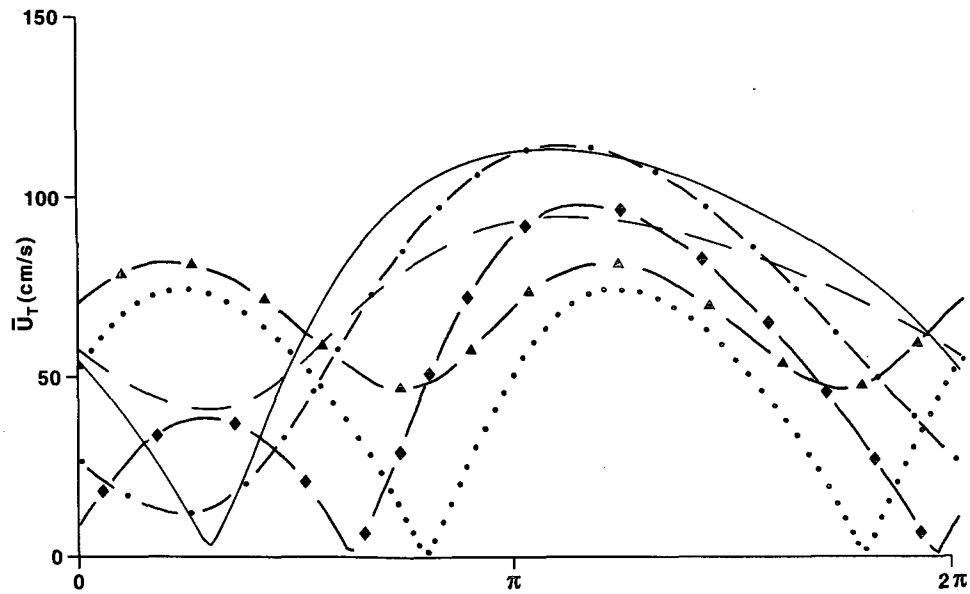

FIG. 9b. As in Fig. 9a but for $\bar{u}_T = (\bar{u}^2 + \bar{v}^2)^{1/2}$.

tide) is always positive (Fig. 9a), giving rise to the time variation of eddy viscosity shown in Fig. 9c.

Profiles of the amplitude of the u and v components of the residual current denoted (D_0); at the forcing period denoted (D_2), at the first harmonic (D_4), and second harmonic (D_6) obtained from a harmonic analysis after a periodic steady state had been reached are shown in Fig. 10a.

A strong, direct wind-driven flow is clearly evident in the u component of the residual current, characterized by a surface wind-driven layer, with a high shear, frictionally retarded bottom boundary layer in which the current falls to zero. Since the eddy viscosity varies with time (Fig. 9c), and current shear $\partial u/\partial z$ is nonzero in this problem, then the nonlinearity arising from the product of these two terms can give rise to an additional *nondirect* wind-driven residual D_0 (a nonlinear tidal residual due to the nonlinear viscosity term), besides the higher harmonics D_4 and D_6. The u component of this tidal residual will be "masked" by the wind-driven

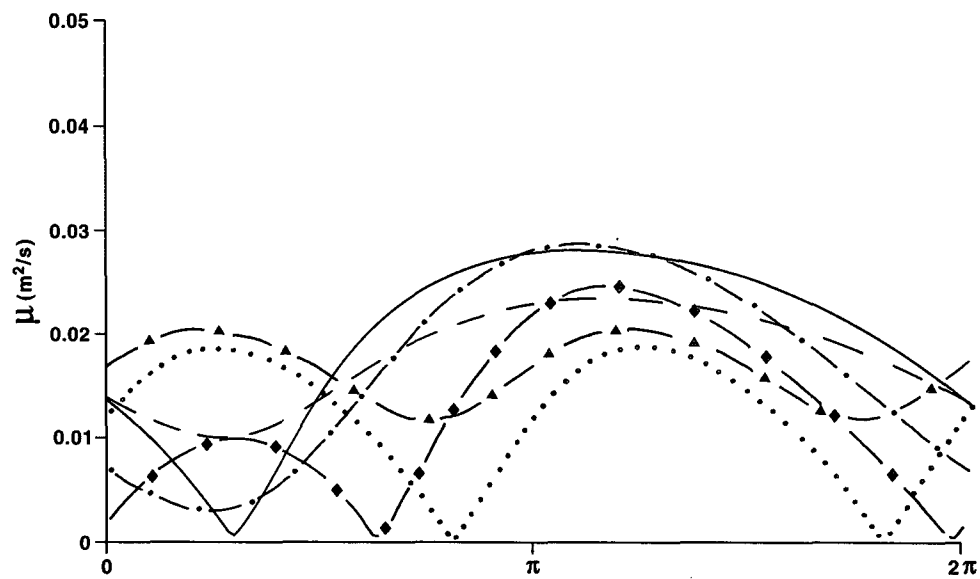

FIG. 9c. As in Fig. 9a but for eddy viscosity μ.

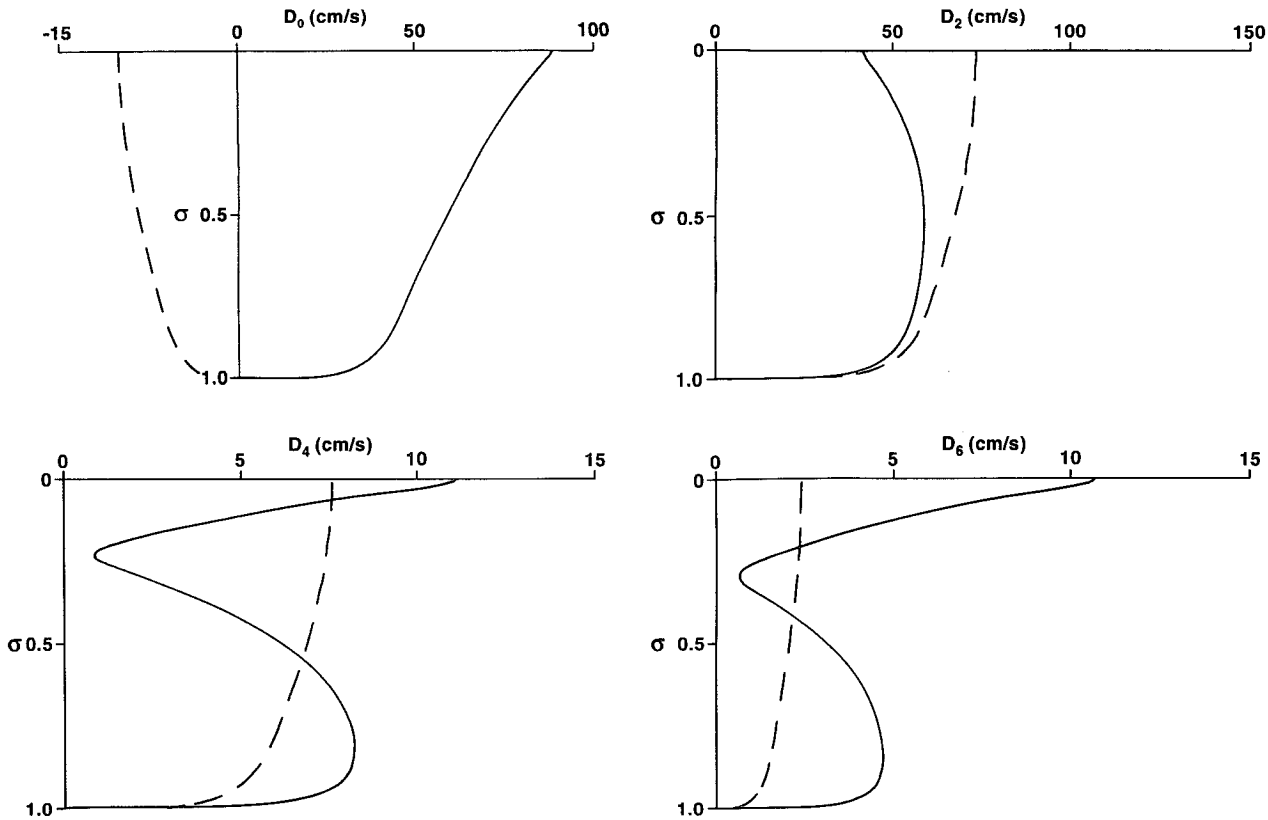

FIG. 10a. Profiles of the amplitude (cm s^{-1}) of the u component (solid) and v component (dashed) of current at the D_0, D_2, D_4, and D_6 frequencies, computed with a circular tidal current ellipse and wind stress F_s = 1.0 N m^{-2}, G_s = 0.0 (calculation 1).

flow but does appear as a small residual in the v component of flow (Fig. 10a).

The profile of the v component of the flow at the forcing frequency D_2 is characteristic of a tidal current, exhibiting an almost shear-free profile in the upper half of the water column, with a decrease close to the seabed. The profile of the u component of the flow (Fig. 10a) at the D_2 frequency (the component aligned with the wind) shows a significant reduction in the surface region, with a midwater maximum, although below midwater the profile is similar to that found for the v component of the tide. Higher harmonics at both the D_4 and D_6 frequency are generated as products of the time-varying viscosity and vertical shear. The presence of wind forcing in the u direction increases shear in the surface and bed boundary layers, giving rise to an increase in the u component of the M_4 tidal current in these boundary layers, above that found for the v component (Fig. 10a).

To examine the sensitivity of the nonlinear term that produces an enhancement in the D_4 and D_6 constituents close to the sea surface, the calculation was repeated using viscosity profiles C and D (calculations 2 and 3, Table 3) with μ_2 = 0.05 (a reduction in near-surface viscosity) and μ_2 = 0.2 (an increase in near-surface viscosity), with μ_1 and μ_0 as before. Reducing the near-surface eddy viscosity increased the near surface shear in the u component of the wind residual and reduced the magnitude of this component of the tide at the D_2 frequency close to the surface with a significant increase in the magnitude of the surface D_4 and D_6 components of the tide (Fig. 10b). An increase in surface eddy viscosity (profile D) lead to a decrease in u components of the D_4 and D_6 tides (Fig. 10b) but an increase in the D_2 component. The v component of the currents at the D_0, D_2, D_4, and D_6 frequencies was not significantly affected by changes in surface eddy viscosity. The decrease in the surface u component of the D_2 tide and the increase in the D_4 and D_6 components with reduced surface viscosity, with little change in the surface wind-driven current, suggests that energy from both the D_2 component of the tide and from the wind-driven flow is transferred into the D_4 and D_6 tidal frequencies as a result of the nonlinearity produced by the time-varying eddy viscosity and surface shear.

To examine the influence of wind strength upon the magnitude of the D_4 and D_6 components of the tide,

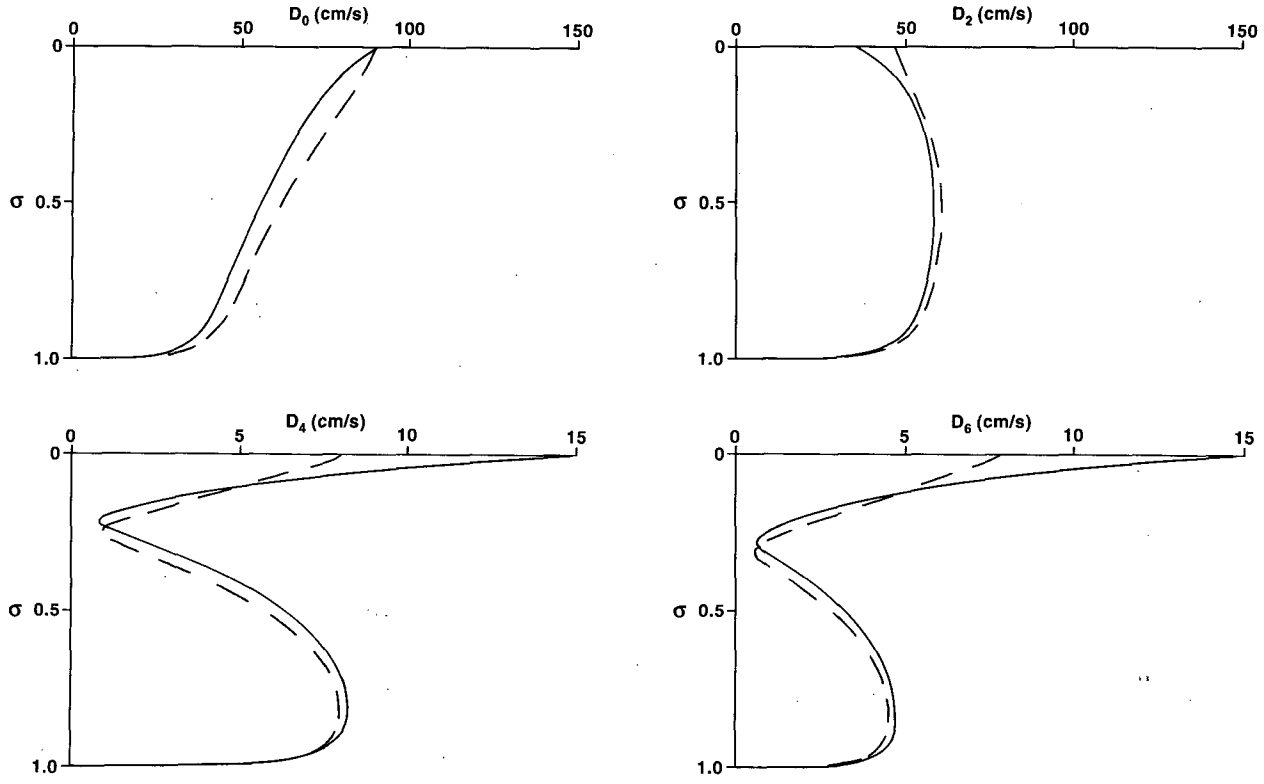

FIG. 10b. Profiles of the amplitude (cm s^{-1}) of the u component of current at the D_0, D_2, D_4, and D_6 frequencies computed with identical tidal and wind forcing as in Fig. 10a but with viscosity profile C (solid) calculation 2 and profile D (dashed) calculation 3.

the previous calculation with viscosity profile B was repeated with $F_x = 0.5$, $G_x = 0.0$ N m^{-2} (calculation 4, Table 3). The time series of depth-mean u current (the component in the wind direction), and $(\bar{u}^2 + \bar{v}^2)^{1/2}$ together with the eddy viscosity (Figs. 9a–c) shows significantly less time variability, with a reduction in the magnitude of the D_4 and D_6 components of the tide from the order of 11 cm s^{-1} (Fig. 10a) to 4 cm s^{-1} for D_4 and below 1.0 cm s^{-1} for D_6. Obviously, the magnitude of surface eddy viscosity and its time variability are important in determining the near-surface shear production of the D_4 and D_6 harmonics.

In a second series of calculations [calculations 5–9, Table 3] the sensitivity to time variations in eddy viscosity was examined using a rectilinear flow in the u direction forced with $h_x = 1.0$ m s^{-1}, $h_y = 0.0$ and $g_x = 0.0$, $g_y = 0.0$. In the case of a pure tidal flow, the depth-mean current in the u direction changes from the order of −80 to +80 cm s^{-1} (with the v component zero) over a tidal cycle (Fig. 9a). The corresponding eddy viscosity time series (Fig. 9c) shows two maxima and two zero values in a tidal cycle corresponding to the maximum tidal current and the times when the current magnitude $(\bar{u}^2 + \bar{v}^2)^{1/2}$ is zero (Fig. 9b).

The addition of a wind stress aligned with the major axis in the u direction, namely, $F_s = 1.0$ N m^{-2}, $G_s = 0.0$, gives a total depth-mean current $\bar{u}$ that remains positive (Fig. 9a) and an associated $(\bar{u}^2 + \bar{v}^2)^{1/2}$ and eddy viscosity having a single maximum and minimum per tidal cycle (Figs. 9b,c). As in the previous case of a circular tidal current ellipse, the direct wind-driven residual (D_0: Fig. 10c) shows a surface shear layer, with the D_2 tidal harmonic indicating a reduced surface current (Fig. 10c) with increases in the D_4 and D_6 harmonics in the near-surface and near-bed layers.

However, in contrast to the calculation using a circular current ellipse, the addition of a reduced wind stress $F_s = 0.5$ in the u direction (calculation 7, Table 3) leads to an enhancement in the magnitude of the D_4 and D_6 harmonics at the sea surface (Fig. 10c). The reason for this is that when a reduced wind stress is added, the depth-mean u component of current is no longer always positive but changes sign over a tidal cycle (Fig. 9a), giving rise to a $(\bar{u}^2 + \bar{v}^2)^{1/2}$ and an associated eddy viscosity that has two maxima and two zero values within a tidal cycle (Fig. 9c). A Fourier analysis of this viscosity time series revealed much larger magnitudes at the D_4 and D_6 period than in the earlier time series. However, when the same wind stress is added at right angles to the major axis, namely, $F_s = 0.0$, $G_s = -0.5$ N m^{-2}, corresponding to a northerly wind stress (calculation 8), then although the u com-

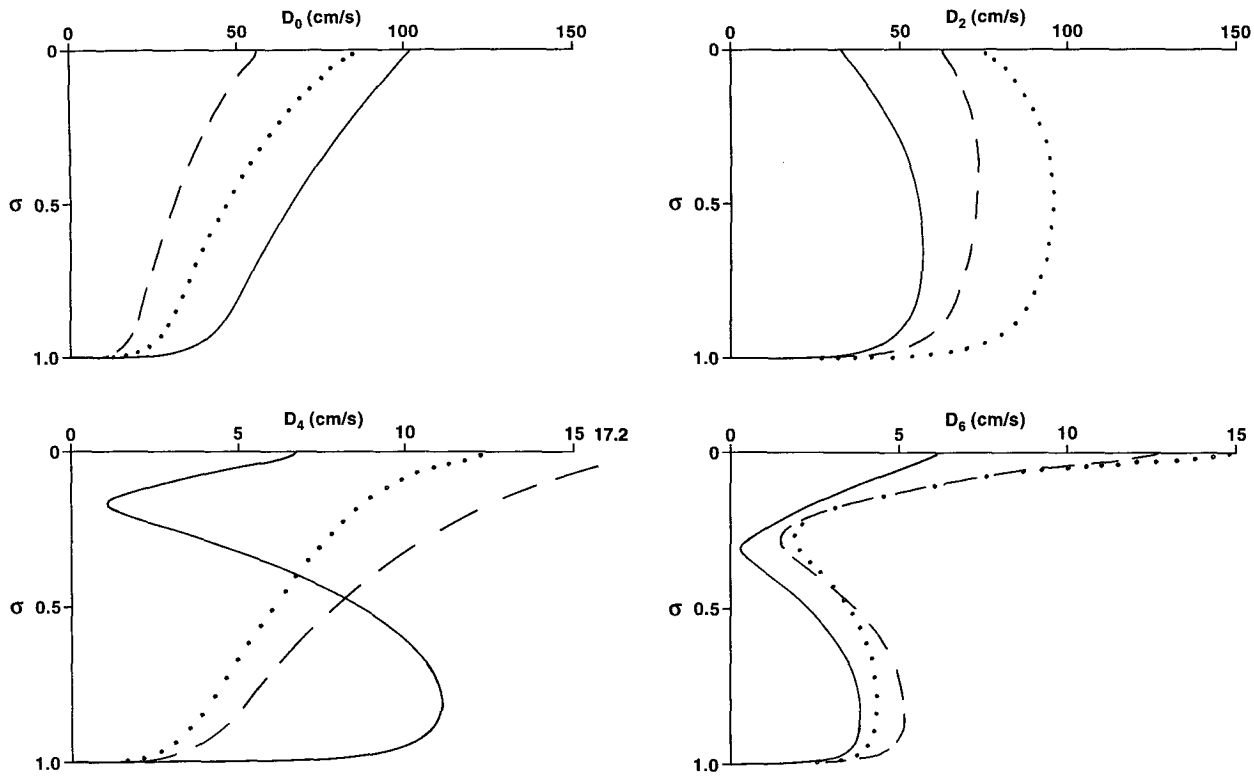

FIG. 10c. Profiles of the amplitude (cm s^{-1}) of the u component of current at the D_0, D_2, D_4, and D_6 frequencies computed using a rectilinear tide and a wind stress: (i) F_s = 1.0 N m^{-2}, G_s = 0.0, h = 10 m (solid) calculation 6; (ii) F_s = 0.5 N m^{-2}, G_s = 0.0, h = 10 m (dashed) calculation 7; and (iii) F_s = 1.0 N m^{-2}, G_s = 0.0, h = 30 m (dotted) calculation 9.

ponent of current changes sign (Fig. 9a), the additional v component due to the wind gives a total current magnitude $(u^2 + v^2)^{1/2}$ with little time variation (Fig. 9b), and the eddy viscosity only shows a slight time variability (Fig. 9c) and the resulting D_4 and D_6 current magnitudes are reduced to the order of 2 cm s^{-1}.

In deeper water h = 30 m (approximately the average of the depths at points B, E, F); with a circular tidal current ellipse the generation of the D_4 and D_6 harmonics is not as large as in shallow water. Since the eddy viscosity in the model is proportional to hu, then for a given tidally forced velocity u, the eddy viscosity increases with h, reducing vertical shear. In the case of the three-dimensional Irish Sea model, in general as h increases, tidal current strength decreases, hence eddy viscosity is much lower than in the single-point model and wind-induced shear would be larger.

In the case of a rectilinear tidal current ellipse (calculation 9, Table 3), in deep water a larger wind stress (F_s = 1.0 N m^{-2}, G_s = 0.0) is required to produce comparable depth-mean currents to those found previously in shallow water (i.e., h = 10 m, with F_s = 0.5 N m^{-2}, G_s = 0.0). Also, in deeper water the model takes longer to reach a periodic condition, and as a check on this, time series of the depth-mean u component of current $\bar{u}$, current magnitude $(\bar{u}^2 + \bar{v}^2)^{1/2}$, and viscosity over two tidal cycles are shown in Fig. 11. Referring to this figure, it is clear that a sinusoidal solution repeated from one tidal cycle to another has been obtained in the model, with current velocity and magnitude comparable to those found previously, in shallow water with the reduced wind stress of 0.5 N m^{-2}. The depth-mean $\bar{u}$ current reaches a maximum value of order 140 cm s^{-1} due to the additional wind-induced velocity with a minimum of −40 cm s^{-1}, giving rise to the time series of current magnitude and viscosity shown in Fig. 11. The maximum eddy viscosity is, however, much larger than those found in the previous calculations with h = 10 m due to the viscosity dependence upon hu. Despite the increased eddy viscosity in deeper water, profiles of D_0, D_2, D_4, and D_6 are similar (Fig. 10c) to those found in shallow regions, with the D_6 surface current in this particular example larger than the D_4 component.

Calculations using a u^2-dependent viscosity [Eq. (9)] show similar profiles of the D_4 and D_6 harmonics generated by identical mechanisms, namely, a time-varying eddy viscosity and a surface shear layer, to those described here.

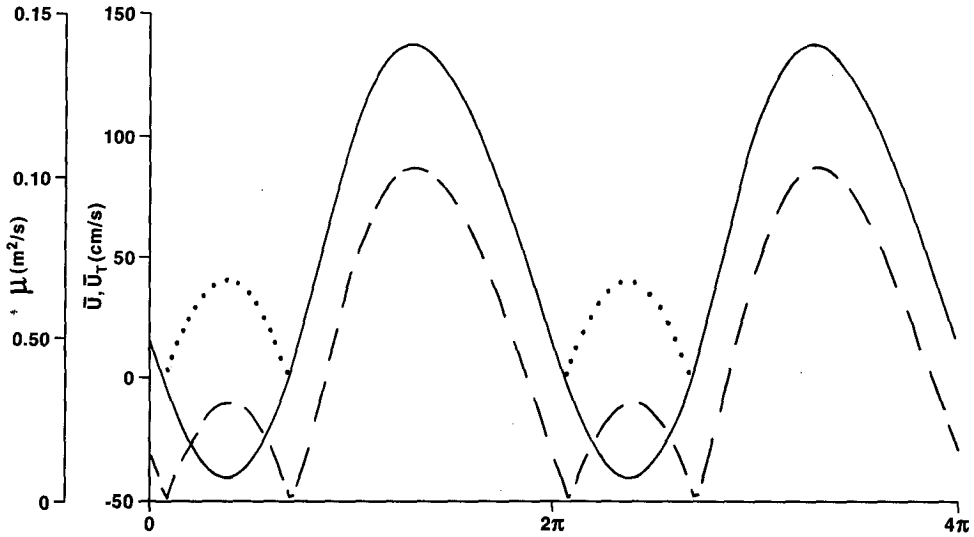

FIG. 11. Time series over two tidal cycles in a water depth $h = 30$ m (calculation 9) of (a) $\bar{u}$ depth-mean current (solid), (b) magnitude of the depth-mean current $\bar{u}_T$ (dotted), and (c) magnitude of the vertical eddy viscosity (dashed).

The addition of rotational effects (i.e., $\gamma \neq 0$), which are important in tidal flow, and quadratic bottom friction, significant in the tidal model, although providing additional coupling between the u and v components of velocity and additional mechanisms for generating the D_4 and D_6 harmonics, do not significantly influence the main findings of the simple-point model. The principal results from the simple-point model suggest that it is the product of the time-varying eddy viscosity and wind-produced shear that are the important mechanisms producing the higher harmonics D_4 and D_6. Since the time variation of the eddy viscosity is produced by the time-varying wind and tidal flows, then the magnitude of these two components of the flow and the alignment of tidal and wind-driven currents are particularly important. The calculations also show that wind-induced shear in the surface layer, which depends upon the magnitude of the near-surface viscosity, is also important.

Recent calculations (Davies and Lawrence 1993) using both a functional approach and finite-difference grids in the vertical, have clearly shown the importance of accurately resolving the vertical shear in determining the extent of the nonlinear coupling. Also, calculations presently being performed with a two-equation turbulence closure model of a form similar to that described in Blumberg and Mellor (1987) also show the nonlinear coupling; results from this type of model will be reported subsequently.

7. Concluding remarks

In this paper we have presented very briefly the major steps in the formulation of a three-dimensional shallow sea model using a finite-difference approach in the horizontal and a spectral method in the vertical; with references to the literature for a more complete description of the formulation. The model includes a flow-dependent eddy viscosity with a quadratic bottom friction formulation that can account for enhancement in the drag coefficient due to wave–current interaction.

Calculations of tidal and wind-induced currents in combination, in a shallow near-coastal region (the eastern Irish Sea where water depths are below 50 m) clearly illustrate that M_2 tidal elevation amplitudes and phases in the near-coastal region are significantly influenced by enhanced levels of turbulence and bed friction associated with the wind-driven circulation. Additional bottom friction due to wind wave turbulence at the seabed also affects tidal elevations.

An examination of the M_2, M_4, and M_6 tidal current profiles in deep and shallow regions reveals that in deep water some slight changes in the profile of the M_2 tidal current amplitude occur when wind forcing is included with significant changes, namely, a reduction of the near-surface tidal current in shallow near-coastal regions. Enhancements in the near-surface M_4 and M_6 components of the tide are found to occur when wind forcing is present. By using a single-point model in the vertical, with a no-slip bottom boundary condition and all nonlinear terms removed, other than those arising with a time-varying eddy viscosity, similar changes in the M_2, M_4, and M_6 tidal currents to those found in the full three-dimensional model were obtained.

Calculations using the single-point model revealed that enhancements in the M_4 and M_6 near-surface tidal currents were produced as a product of the time-varying

eddy viscosity and wind-induced shear, with the greatest changes occurring in shallow water regions.

In this paper we have considered a large wind stress, typical of a major storm event. Under more moderate wind conditions the wind-driven flow will be reduced and hence the contribution of the wind-forced turbulence will be less, although the nonlinear nature of the processes concerned suggests that a simple linear reduction is unlikely to occur. Also the wave–current interaction effects depend very much upon the nature of the wind waves, with swell enhancing the level of wave–current interaction significantly in deep water. Since the wind wave spectrum depends very much upon wind duration and fetch and not simply wind magnitude, then the level of wave–current interaction will not depend in a simple manner upon wind stress.

The calculations presented in this paper suggest that during a major wind event, significant changes in M_2 tidal elevation, and M_2, M_4, and M_6 tidal current profiles will occur in shallow near-coastal regions using the flow-dependent eddy viscosity formulation described here. A series of accurate measurements of near-surface currents at the M_2, M_4, and M_6 period during major wind events, with corresponding measurements of bed stress, to determine enhancement due to wave current activity in a nearshore region with significant tidal currents would be very useful in validating the various mechanisms proposed in this paper and appropriate formulations of eddy viscosity. To date no such datasets exist; however, instruments capable of making such measurements have now been developed, and hopefully the ideas proposed in this paper will act as a focus for a near-shore current profile and wind wave measurement program.

Acknowledgments. One author (JL) would like to express his thanks to the director of POL for computing and other facilities during his stay and to MAFF for a year's leave of absence.

The authors are indebted to R. A. Smith for preparing diagrams and J. Hardcastle for typing the paper.

REFERENCES

Aldridge, J. N., and A. M. Davies, 1993: A high-resolution three-dimensional hydrodynamic tidal model of the eastern Irish Sea. *J. Phys. Oceanogr.*, **23,** 207–224.

Amin, M., 1982: On analysis and forecasting of surges on the west coast of Great Britain. *Geophys. J. Roy. Astron. Soc.*, **68,** 79–94.

Bowden, K. F., 1978: Physical problems in the benthic boundary layer. *Geophys. Surveys,* **3,** 255–296.

——, and S. R. Ferguson, 1980: Variations with height of the turbulence in a tidally-induced bottom boundary layer. *Marine Turbulence,* J. C. J. Nihoul, Ed., Elsevier, 259–286.

——, L. A. Fairbairn, and P. Hughes, 1959: The distribution of shearing stresses in a tidal current. *Geophys. J. Roy. Astron. Soc.*, **2,** 288–305.

Blumberg, A. F., and G. L. Mellor, 1987: A description of a three-dimensional coastal ocean circulation model. *Three-Dimensional Coastal Ocean Models,* N. S. Heaps, Ed., Amer. Geophys. Union, 1–16.

Carter, D. J. T., 1982: Prediction of wave height and period for a constant wind velocity using the Jonswap results. *Ocean Eng.*, **9,** 17–33.

Christoffersen, J. B., and I. G. Jonsson, 1985: Bed friction and dissipation in a combined current and wave motion. *Ocean Eng.*, **12,** 387–423.

Davies, A. G., 1986: A numerical model of the wave boundary layer. *Contin. Shelf Res.*, **6,** 715–739.

——, 1990: A model of the vertical structure of the wave and current bottom boundary layer. *Modeling Marine Systems,* Vol. 2, A. M. Davies, Ed., CRC Press, 263–297.

——, 1991: Transient effects in wave-current boundary layer flow. *Ocean Eng.*, **18,** 75–100.

——, R. L. Soulsby, and H. L. King, 1988: A numerical model of the combined wave and current bottom boundary layer. *J. Geophys. Res.*, **93,** 491–508.

Davies, A. M., 1982: Meteorologically-induced circulation on the north west European continental shelf: From a three-dimensional numerical model. *Oceanol. Acta,* **5,** 269–280.

——, 1986: A three-dimensional model of the northwest European continental shelf, with application to the M_4 tide. *J. Phys. Oceanogr.*, **16,** 797–813.

——, 1987: Spectral models in Continental Shelf sea oceanography. *Three-Dimensional Coastal Ocean Models,* N. S. Heaps, Ed., Amer. Geophys. Union, 71–106.

——, 1990: On the importance of time varying eddy viscosity in generating higher tidal harmonics. *J. Geophys. Res.*, **95,** 20 287–20 312.

——, 1991: On using turbulence energy models to develop spectral viscosity models. *Contin. Shelf Res.*, **11,** 1313–1353.

——, 1993: A bottom boundary layer–resolving three-dimensional tidal model: A sensitivity study of eddy viscosity formulation. *J. Phys. Oceanogr.*, **23,** 1437–1453.

——, and R. A. Flather, 1977: Computation of the storm surge of 1–6 April 1973 using numerical models of the north west European continental shelf and North Sea. *Dtsch. Hydrogr. Z.*, **30,** 139–162.

——, and C. V. Stephens, 1983: Comparison of the finite difference and Galerkin methods as applied to the solution of the hydrodynamic equations. *Appl. Math. Modelling,* **7,** 226–240.

——, and R. A. Flather, 1987: Computing extreme meteorologically induced currents, with application to the northwest European continental shelf. *Contin. Shelf Res.*, **7,** 643–683.

——, and J. E. Jones, 1992a: A three dimensional model of the M_2, S_2, N_2, K_1, and O_1 tides in the Celtic and Irish Seas. *Progress in Oceanography,* Vol. 29, Pergamon, 197–234.

——, and ——, 1992b: A three dimensional wind driven circulation model of the Celtic and Irish Seas. *Contin. Shelf Res.*, **12,** 159–188.

——, and J. N. Aldridge, 1993: A numerical model study of parameters influencing tidal currents in the Irish Sea. *J. Geophys. Res. (Oceans),* **98,** 7049–7067.

——, and J. Lawrence, 1993: Modelling the non-linear interaction of wind and tide: Its influence on current profiles. *Int. J. Numer. Meth. Fluids,* **18,** 163–188.

——, and ——, 1994: A wind driven high resolution model of the eastern Irish Sea, including wave–current interaction. *J. Phys. Oceanogr.*, submitted.

Draper, L., 1992: *Wave Climate of the British Isles.* HMSO, 1–36. [ISBN 011 4130 92 2.].

Dyke, P. P. G., 1977: A simple ocean surface layer model. *Riv. Ital. Geofis.*, **4,** 31–34.

Furnes, G. K., 1983: A three dimensional numerical sea model with eddy viscosity varying piecewise linearly in the vertical. *Contin. Shelf Res.*, **2,** 231–242.

Grant, W. D., and O. S. Madsen, 1979: Combined wave and current interaction with a rough bottom. *J. Geophys. Res. (Oceans),* **84,** 1797–1808.

——, and ——, 1986: The continental-shelf bottom boundary layer. *Annu. Rev. Fluid. Mech.*, **18,** 265–305.

Green, M. O., J. M. Rees, and N. D. Pearson, 1990: Evidence for the influence of wave-current interaction in a tidal boundary layer. *J. Geophys. Res.*, **95,** 9629–9644.

Heathershaw, A. D., 1981: Comparison of measured and predicted sediment transport rates in tidal currents. *Mar. Geol.*, **42,** 75–104.

Huntley, D. A., and A. J. Bowen, 1990: Modeling sand transport on continental shelves. *Modeling Marine Systems,* A. M. Davies, Ed., CRC Press, 221–254.

Jonsson, I. G., 1967: Wave boundary layers and friction factors. *Proc. Tenth Int. Conf. on Coastal Engineering,* New York, NY, Amer. Soc. Civ. Eng., 127–148.

——, and N. A. Carlsen, 1976: Experimental and theoretical investigations in an oscillatory turbulent boundary layer. *J. Hydraulic Res.*, **14,** 45–60.

Le Provost, C., and M. Fornerino, 1985: Tidal spectroscopy of the English Channel with a numerical model. *J. Phys. Oceanogr.*, **15,** 1009–1031.

Lynch, D. R., and F. E. Werner, 1991: Three-dimensional velocities from a finite-element model of English Channel/Southern Bight tides. *Tidal Hydrodynamics,* B. B. Parker, Ed., Wiley & Sons, 183–200.

Proctor, R., 1981: Tides and residual circulation in the Irish Sea: A numerical modelling approach. Ph.D. thesis, Liverpool University, 1–254.

——, 1987: A three dimensional numerical model of the eastern Irish Sea. *Numerical Modelling: Application to Marine Systems,* J. Noye, Ed., Elsevier, 25–45.

——, and R. A. Flather, 1988: Storm surge prediction in the Bristol Channel—the floods of 13 December 1981. *Contin. Shelf Res.*, **9,** 889–918.

——, and J. Wolf, 1989: An investigation of the storm surge of 1 February 1983, using numerical models. *Modeling Marine Systems,* A. M. Davies, Ed., CRC Press, 43–72.

Signell, R. P., R. C. Beardsley, H. C. Graber, and A. Capotondi, 1990: Effect of wave–current interaction on wind-driven circulation in narrow, shallow embayments. *J. Geophys. Res.*, **95,** 9671–9678.

Spaulding, M. L., and T. Isaji, 1987: Three dimensional continental shelf hydrodynamic model including wave current interaction. *Three-Dimensional Models of Marine and Estuarine Dynamics,* J. C. J. Nihoul and B. M. Jamart, Eds., Elsevier, 405–426.

Walters, R. A., and F. E. Werner, 1989: A comparison of two finite element models of tidal hydrodynamics using a North Sea data set. *Advances in Water Resources,* Vol. 12, Elsevier, 184–193.

Wolf, J., 1980: Estimation of shearing stresses in a tidal current with application to the Irish Sea. *Marine Turbulence,* J. C. J. Nihoul, Ed., Elsevier, 319–344.